Transitioning Between Theory and Observations of Strongly Magnetized Accreting Neutron Stars: A Blinded Synthetic Data Study

Research Project Report

Nureldin Schettino

Dr. Karl-Remeis Sternwarte
Friedrich-Alexander Universität
Erlangen-Nürnberg

Supervisor:
Dr. Ekaterina Sokolova-Lapa

February, 2026

Abstract

The magnetic fields of accreting X-ray pulsars (XRPs) are among the most powerful in the universe and control the extreme accretion physics that shape XRP spectra. Spectral analysis therefore provides a direct probe of XRP physics; in particular, cyclotron resonant scattering features yield measurements of the magnetic field strength. However, cyclotron lines are often difficult to identify and fit with purely phenomenological models, and physically motivated spectral models can help clarify their formation and shapes.

In an attempt to connect theory and observation, I performed an analysis of nine highly magnetized accreting XRP spectra which were blinded prior to the analysis. Five of these spectra were revealed to be synthetic after unblinding. I show how physical interpretation of phenomenological models can be bias-prone by comparing phenomenological fits to model-defined input parameters. I find that achieving acceptable phenomenological fits frequently requires adding artefactual emission or absorption components. Such spurious components are evident in the residuals and can mimic cyclotron lines, potentially biasing physical interpretation. I discuss the implications for accreting XRP phenomenological analysis and the roles of physical models in interpreting emergent emission.

Contents

1 Introduction

Neutron stars are among the most strongly magnetized objects in the universe and serve as natural laboratories for extreme physics, including accretion in binary systems. Their intense magnetic fields govern the dynamics of the accretion flow and shape the emergent X-ray emission. Although surface B-field strengths for isolated radio pulsars can be estimated via the neutron star's spin period P and its time derivative $\dot{P}$ under the assumption of magnetic-dipole emission (Lorimer & Kramer 2012), this is not directly applicable to accreting systems. Consequently, spectral analysis – particularly of accreting X-ray pulsars (XRPs) – provides more precise tools for localized magnetic field measurement.

Cyclotron resonance scattering features (CRSFs; sometimes called "cyclotron lines"), first discovered by Trümper et al. (1978), are central to this toolkit, serving as direct probes of magnetic field strength in the line-formation region (Staubert et al. 2019). However, identifying and fitting these features phenomenologically has been challenging due to instrumental limitations in sensitivity and energy resolution, as well as broadening and shifting effects that depend on plasma temperature, vacuum polarization, accretion and observational geometry, and mass-accretion rate.

These challenges motivate this project, where I performed a blinded analysis of nine *NuSTAR* spectra of highly magnetized accreting XRPs in high-mass X-ray binaries (HMXBs). This analysis has two primary goals: first, during the blinded phase, I carried out unbiased characterizations of the high-energy spectra with particular emphasis on features like the aforementioned CRSFs. Second, after unblinding, five of the nine spectra were revealed to be synthetic spectra, allowing me to test how well my fits recover known model parameters.

By comparing my fits with prior literature for the real spectra and with model-defined input parameters for the synthetic spectra, I assess the impact of confirmation bias based on prior results from peer-reviewed publications and the risk of misidentifying spectral features driven by specific assumptions about spectral formation. To this end, this project connects physical modeling to spectral analysis, highlighting how physical interpretation may be bias-prone or model-dependent.

The remainder of Section 1 discusses the relevant accretion physics, spectral formation, and CRSFs. Section 2 describes the sources and my analyses thereof. Section 3 presents my fit results and a blinded comparative analysis of the spectra. Section 4 covers the unblinding procedure, compares my fit parameters to model-defined input parameters, reviews physical continuum modeling in the field, and describes the `sigel-T` model. Finally, Section 5 briefly summarizes findings, presents conclusions, and discusses the outlook on future applications.

1.1 The Physics of Accretion and Spectral Formation

Most accretion powered X-ray pulsars fall into two main varieties distinguished based on their companion's mass: high-mass X-ray binaries (HMXBs) and low-mass X-ray binaries (LMXBs) (Caballero & Wilms 2012). Each type of X-ray binary (XRB) is generally associated with distinct accretion mechanisms. Since the most highly magnetized accreting neutron stars are typically found in HMXBs, I will focus on that class. LMXBs typically host magnetically weaker systems which are less relevant to the phenomena I examine in this project.

As a general rule, the X-ray emission of accreting XRBs is powered by the gravitational energy released during accretion. Conservation of angular momentum requires that the matter not fall directly onto the neutron star's surface. Therefore, different combinations of the binary system's geometry and stellar companion's properties lead to diverse accretion mechanisms. This report will focus on radiative properties close to the neutron star's surface since these best explain continuum formation and specific spectral features like CRSFs.

HMXBs are sub-categorized based on the companion's stellar type. These companions can be massive O/B stars or Be stars. The former are typically associated with traditional wind accretion mechanisms, whereas the latter are transient systems where mass transfers from a decretion disk around the Be star to an accretion disk around the neutron star. It is assumed that mass transfer takes place when the neutron star approaches the Be star during periastron passage.

O/B stellar systems exhibit particularly strong winds, with mass loss rates as high as $\dot{M} \sim 10^{-4} - 10^{-6} M_{\odot}/\mathrm{yr}$. Their neutron stars are typically embedded in the stellar wind due to their close orbits. Be systems exhibit eccentric orbits that result in transient behavior. This can manifest as giant (type II) or normal (type I) outbursts punctuated by quiescent periods of varying length dependent on orbital period and mass loss rate.

1.1.1 Accretion Flow and Characteristic Radii

The innermost accretion flow dynamics of HMXBs are dominated by the neutron star's strong magnetic field (typically of order $B \sim 10^{12}\,\mathrm{G}$) such that the infalling matter is funneled along magnetic field lines onto the neutron star's magnetic poles (Caballero & Wilms 2012). The matter is first disrupted by the neutron star's magnetic field at the magnetospheric radius r_{m}. A closely related scale is the Alfvén radius r_{a} (typically thousands of kilometers from the neutron star), the characteristic radius at which the accreted matter's inward ram pressure and the magnetic field's outward magnetic pressure are in equilibrium such that the matter effectively couples to the magnetic field. These radii, r_{m} and r_{a}, are related by some coefficient of proportionality Λ such that

$$r_{\mathrm{m}} = \Lambda r_{\mathrm{a}}. \tag{1}$$

This coefficient depends on a system's exact accretion flow geometry and is assumed to be ~ 1 for spherical geometries.

Inside the Alfvén radius, the dynamics are magnetically dominated, and the flow follows the field lines. However, as shown by Ghosh & Lamb (1979), the plasma and neutron star angular velocities can differ based on the plasma's distance from the neutron star. We define the co-rotation radius r_{co} as the point at which the plasma and neutron star angular velocities are equal. If $r_{\mathrm{a}} > r_{\mathrm{co}}$, accretion can be inhibited at the magnetospheric radius r_{m}, where the magnetosphere acts as a centrifugal barrier for the infalling matter.

1.1.2 Accretion Regimes and the Accretion Column

Infalling matter approaches the neutron star's magnetic poles at near-relativistic speeds ($\sim 0.7c$) where it is brought to rest and radiates its kinetic energy away. The matter's deceleration mechanism depends on the mass accretion rate $\dot{M}$ which we infer from the radiation emitted in the deceleration region.

We classify deceleration scenarios into luminosity-dependent accretion regimes that produce distinct diagnostic spectral features. Following Basko & Sunyaev (1976), we categorize accretion regimes into the low and high mass accretion scenarios. At low $\dot{M}$, correspondingly low radiation pressure leads to accretion flow deceleration by (i) Coulomb collisions at the neutron star's atmosphere or (ii) collisionless shock above its surface. At high $\dot{M}$, radiation pressure decelerates the material above the neutron star's surface in a radiation-dominated shock (iii). We call the luminosity at which radiation pressure can stop accretion flow above the surface "critical", denoted by L_{crit}. At super-critical luminosities ($L > L_{\mathrm{crit}}$), radiation shock is expected to form an emitting structure called the accretion column. Figure 2 is a schematic illustration of such a column, outlining its internal structure with respect to various radiative mechanisms.

Accretion column structure remains a largely unsolved, though actively studied, problem in the physics of accreting XRPs. Its complexity arises from the strong coupling between matter and radiation in the accretion channel, whose geometry determines the column structure. The column's presence can be ascertained via the neutron star's pulse profile because it is influenced by the emission beam pattern, itself determined by the matter deceleration mechanism at play. Observations of accreting X-ray pulsars over a range of luminosities can therefore offer a glimpse into changes in emission region geometry.

1.1.3 Emission Mechanisms and Spectral Formation

There currently exists no self-consistent physical spectral formation model applicable to all accretion regimes. Nevertheless, those models which do exist provide guidance for interpreting phenomenological spectral fits to observational data.

Photon scattering cross sections are strongly polarization-dependent in highly magnetized accreting XRPs, so the radiation emerging from the emission region is expected to be highly polarized and anisotropic (Sokolova-Lapa et al. 2023). Photon polarization separates into two normal modes: the ordinary, O, and extraordinary, X. These polarization modes, together with the luminosity (hence $\dot{M}$) and the local magnetic geometry, determine whether the net beam pattern is predominantly fan or pencil-like (Basko & Sunyaev 1975). In terms of $\dot{M}$, a super-critical accretion regime produces an accretion column whose sides emit a fan beam, whereas a sub-critical flow produces more pencil-like emission from the top of a much shorter column-like structure or, in its absence, a polar hot spot (Becker et al. 2012). Further, beam pattern changes produce characteristic signatures in neutron star pulse profiles. When used together with luminosity measurements (which trace $\dot{M}$) and complementary tools and diagnostics (like phase-resolved spectroscopy and cyclotron line behavior) they can help infer the presence of an accretion column and constrain the accretion regime.

The key physical ingredients governing spectral formation are the geometry of the emission region, which we know depends on the neutron star's mass-accretion rate; seed photon production, i.e. production of those photons which are upscattered to higher energies; and radiative transfer processes. There have been multiple seminal works that attempt to analytically or numerically derive physical models for spectral formation. Mészaros and Nagel's work (Nagel 1981; Meszaros & Nagel 1985a,b) investigated radiative transfer and spectral formation in magnetized accretion columns, highlighting the role of geometry as well as the effects of polarization and anisotropy on both the continuum's overall shape and on specific spectral features. This study, together with its subsequent extensions, remains directly relevant to modern efforts in physical modeling of accreting XRP spectra, including the model employed in this study.

Becker & Wolff (2007) developed a continuum formation model for super-critically accreting X-ray pulsars that is based on the accretion scenario described by Davidson & Ostriker (1973). The primary processes responsible for spectral formation in this model are bulk and thermal Comptonization of blackbody, bremsstrahlung, and cyclotron seed photon populations. They compare the overall accretion scenario to the "flow of a mixture of gas and radiation" inside a "magnetic pipe" sealed with respect to the gas (i.e. the matter does not escape) but transparent with respect to the radiation (i.e. upscattered seed photons can escape) (Becker & Wolff 2007).

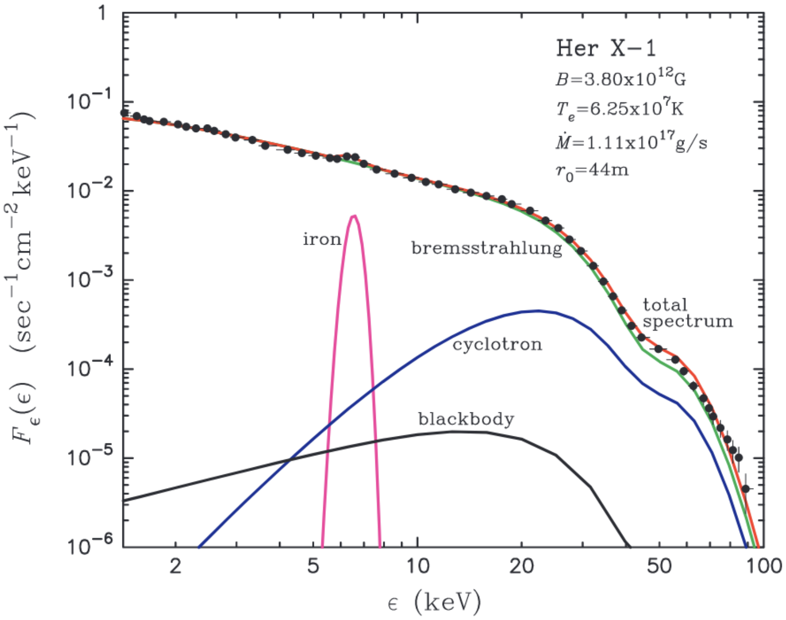

Figure 1: Theoretical spectrum of Her X-1 showing the individual contributions of different emission components to the overall continuum shape. Figure 6 from Becker & Wolff (2007).

In the Becker & Wolff (2007) model, seed photons are produced at the thermal mound, a dense layer of hot plasma that is located on the neutron star's surface at the base of the accretion column (see Fig. 2). Cyclotron and bremsstrahlung seed photons are produced in the optically thin region above. The various seed photon varieties are upscattered to X-ray energies via both bulk Comptonization, where photons gain energy by scattering with infalling electrons experiencing converging flow (Laurent & Titarchuk 1999), and thermal Comptonization, where photons gain energy by scattering off thermal electrons. In the Becker & Wolff model, since the inflow electron speed in the accretion column is significantly larger than thermal velocity, bulk Comptonization dominates except at the highest photon energies, where stochastic thermal processes contribute more strongly. Figure 1 illustrates a theoretical model showing the expected contributions and spectral energies of these processes to the continuum shape.

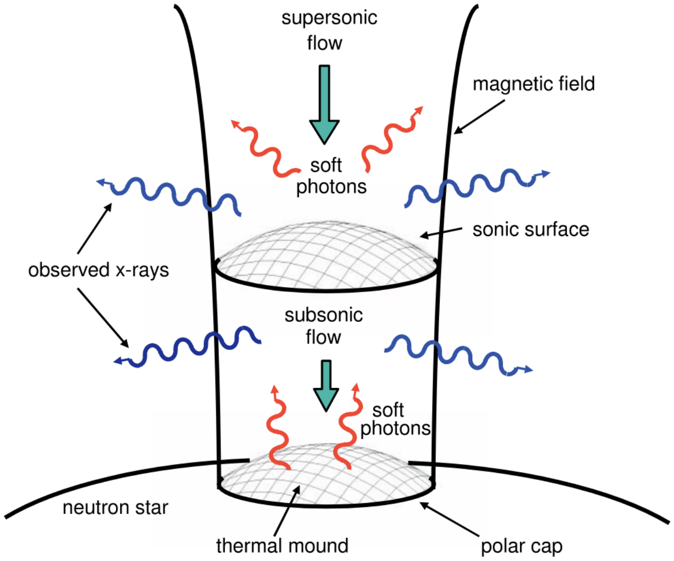

Figure 2: Schematic depiction of the accretion column, showing gas accreting onto the neutron star's magnetic polar cap. Figure 1 from Becker & Wolff (2007).

Mushtukov & Tsygankov (2024) note that given a high $\dot{M}$, additional processes influence spectral formation, particularly the soft X-rays. These include reprocessing of X-rays by accretion flow inside the magnetospheric radius and reprocessing by disc-launched outflows.

Spectral formation for particularly low-luminosity sources in the sub-critical accretion regime is characterized by a double-hump shape observed in low-luminosity

X-ray pulsars (e.g. Sokolova-Lapa et al. 2021). Careful consideration of source luminosity is therefore essential to avoid misidentifying the dip between the two humps as a CRSF. The physical picture in this regime differs fundamentally from the supercritical case, as radiation pressure is insufficient to support the formation of an accretion column. Instead, matter reaches the neutron star surface in free fall and, as discussed in Section 1.1.2, Coulomb interactions are expected to provide the dominant deceleration mechanism.

For especially low-luminosity sources, Sokolova-Lapa et al. (2021) developed a polar-cap model describing continuum formation from the accretion of fully ionized hydrogen plasma at mass accretion rates $\dot{M} \lesssim 10^{15}\,\mathrm{g\,s^{-1}}$ onto the neutron star magnetic poles. Under these conditions, no accretion column is expected to form and the polar cap itself constitutes the emission region. The low-energy spectral hump is thermal in origin and dominated by extraordinary-mode photons, while the high-energy hump is produced by resonant magnetic Comptonization and is further modified by cyclotron line formation. Overall, the spectral morphology arises from strong mode-dependent opacities and atmosphere inhomogeneity. Mushtukov et al. (2021) propose an alternative model, attributing the high-energy component to Comptonized cyclotron photons.

1.1.4 Cyclotron Resonance Scattering Features

One of the neutron star's defining properties, its strong magnetic field, gives rise to a variety of exotic phenomena observable in X-ray spectra. Among these, the most well-studied is the CRSF, whose physical origin and observational properties are discussed here.

CRSFs arise from the quantum electrodynamics of charged particles in strong magnetic fields. In magnetic fields of order $10^{12} - 10^{13}\,\mathrm{G}$ the perpendicular motion of these electrons becomes quantized with discrete energy levels known as Landau levels. The electrons are thus confined to circular orbits of fixed energy in the plane perpendicular to the field while remaining free to move along the field lines. Due to the resonant scattering of photons off of these electrons, absorption-like features can appear in the X-ray spectra of accreting XRPs (Staubert et al. 2019). These are the CRSFs.

The energy spacing between the Landau levels is given by

$$E_{\mathrm{cyc}} = \frac{\hbar e B}{m_{\mathrm{e}} c} = 11.6\,\mathrm{keV} \cdot B_{12}, \tag{2}$$

where B_{12} is the magnetic field in units of 10^{12}G. This equation is also modified to account for gravitational red shift due to the strong gravitational field around the neutron star. This yields

$$E_n = nE_{\rm cyc}(1+z)^{-1} \tag{3}$$

for the nth harmonic where z is the gravitational redshift. Cyclotron line energy therefore provides a direct measurement of the neutron star magnetic field, making CRSFs powerful diagnostic tools to probe the star's accretion structure and dynamics, as well as its plasma properties and luminosity. Their phase dependence also allows us to use them to investigate the effects of scattering cross sections on scattering angles (Wilms 2014). At high electron temperatures ($\gtrsim 5$ keV), cyclotron lines can also exhibit "wings", spectral features that flank the central "dip" that arise from the resonant scattering and photon redistribution mechanisms in the emission region (Sokolova-Lapa et al. 2021; Schwarm et al. 2017b).

Using a multiangle, incoherent scattering formalism in tandem with their slab and cylindrical emission region geometries, Meszaros & Nagel (1985a,b) also show that cyclotron line shape is strongly angle- and polarization-dependent. That is, the width, depth, and apparent centroid energy parameters (displacement from its harmonic energy E_n) of observed cyclotron lines depend on the rotational phase and the redistribution mechanisms at play. Nishimura (2005) also shows that superposition of individual lines can create an asymmetric profile that broadens and deepens the resultant line or makes it appear shallower at lower energies due to the gradient of widths in the original, superposed lines. Given that spectra are phase averaged, this further complicates interpretation of cyclotron line fits. Finally, even though past models for CRSFs on top of predefined continua have often adopted a pure vacuum assumption (Schwarm et al. 2017a,b), quantum electrodynamical effects like vacuum polarization can appreciably alter cyclotron line profiles and even produce weak dips in the continuum that mimic CRSFs (Sokolova-Lapa et al. 2023).

1.2 Phenomenological Spectral Modeling

Because no single physical model currently describes the full parameter range of accreting, highly magnetized X-ray pulsars, we fit continua phenomenologically and interpret results using different physical scenarios appropriate to the expected accretion regime. In practice, a single absorbed powerlaw with a high-energy exponential cutoff of $\sim$ 10–30 keV (Falkner 2018; Müller et al. 2013) provides an adequate broadband description for many sources and luminosities with the notable exception of low-luminosity sources.

Some of the most commonly used phenomenological models include the `XSPEC` high-energy cut off model `cutoffpl`

$$\texttt{cutoffpl(E)} = KE^{-\Gamma}\exp(-E/E_{\rm fold}), \tag{4}$$

where Γ is the photon index, which determines the slope in a log-log scale; E_{fold} is the folding energy, which determines continuum roll-over; and K is the normalization constant which determines the overall flux level. While Γ is often ~ 1, both it and the roll-over energy vary considerably depending on the source.

Tanaka (1986) developed another common choice, a power-law with a Fermi-Dirac cutoff,

$$\texttt{fdcut(E)} = KE^{-\Gamma}[1 + \exp(-(E - E_{\text{cut}})/E_{\text{fold}})]^{-1}. \tag{5}$$

Although both parameters are phenomenological, the cutoff energy E_{cut} is usually interpreted as the onset energy at which physical high-energy attenuation begins to modify the continuum, whereas the rollover or folding energy E_{fold} regulates the steepness/curve of the spectral decline beyond the cutoff, represents the electron temperature, and is expected to scale with E_{cut}.

Mihara (1995) developed a model consisting of a combination of a positive and a negative power-law with an exponential cutoff,

$$\texttt{NPEX(E)} = (K_1 E^{-\Gamma_1} + K_2 E^{-\Gamma_2}) \exp(-E/kT), \tag{6}$$

where T is the plasma temperature of the emitting plasma and k is the Boltzmann constant. This can be understood as two `cutoffpl` models with the same folding energy (Schwarm 2017).

Improved sensitivity and energy resolution have revealed additional continuum complexity that is often modeled with ad hoc components. Examples include the so-called "10 keV feature," a broad Gaussian–like feature with reported centroids in the $\sim$ 8–30 keV range and unclear physical origin. Well-defined spectral features like CRSFs are usually modeled with multiplicative profiles like `gabs` (Gaussian absorption) or `cyclabs` (a pseudo-Lorentzian profile). Note that different CRSF models can produce systematic offsets; for instance, Schwarm (2017) shows that the minimum of a `cyclabs` profile does not always coincide exactly with E_{CRSF}, producing systematic shifts of order 1-4 keV.

2 Methods

2.1 Spectral Sources

I received spectra that were truncated below 8 keV. Accordingly, the synthetic data were adapted to *NuSTAR*, chosen for its extended energy coverage of 3–79 keV. All data resembled *NuSTAR* observations, with corresponding pha and bkg files and appropriate RMF and ARF contributions.

2.2 Blinded Spectral Analysis

Having received pre-extracted and blinded data, my interaction with it was limited to spectral analysis. I used the Interactive Spectral Interpretation System (ISIS), a tool designed for the analysis of X-ray spectra that uses the interpreted scripting language S-lang. I used both local and `XSPEC` models to bin and fit these data. I also used chi-square statistics to evaluate model fit since there were enough counts per bin to satisfy the assumptions of chi-square goodness-of-fit testing.

To model the overall spectral continua, I chose between the `cutoffpl` and `fdcut` models, depending on the object. I consistently began with `cutoffpl` to minimize the number of free parameters; however, in some cases this model could not adequately reproduce the exponential high-energy cutoff. Adjusting the interplay between the folding energy E_{fold} and the photon index Γ sometimes led to steeply negative photon indices ($\Gamma < -2$). In such instances, I adopted the `fdcut` model, whose additional flexibility in normalization, photon index, and cutoff energy yielded parameters within expected ranges.

I did not use `NPEX` because the energy ranges of all the spectra begin at 8 keV, whereas `NPEX` is typically applied to data with softer X-ray coverage. It also uses additional free parameters compared to alternative continuum models. Moreover, previous studies have criticized `NPEX` for producing an apparent anti-correlation between luminosity and cyclotron line energy (Mihara et al. 2004), later shown to arise from unphysical coupling between CRSF parameters and the continuum model (Müller et al. 2013). Given the key role of cyclotron lines in this study, I limited myself to `cutoffpl` and `fdcut` for more physically cogent interpretations.

For cyclotron lines, I used the multiplicative Gaussian model `gabs` rather than `cyclabs`. This choice was driven by practical reasons: `gabs` has fewer free parameters, while `cyclabs` typically requires fitting the first harmonic (adding free parameters) and can shift fitted centroids in ways that complicate physical interpretation (see discussion in 1.2). Furthermore, our spectra are blinded with respect to luminosity, which prevents examining luminosity to distinguish broadened fundamental lines from the dip between spectral humps in low-luminosity sources. A simpler model therefore seemed more appropriate for these conditions.

With regard to binning, I attempted to determine object-specific count minima per bin such that I could fit the full continuum more effectively. After the study's conclusion, I realized that a more appropriate and effective approach involves binning more aggressively to constrain the full continuum shape and prevent narrow spectral features such as the 10-keV bump or broadened cyclotron lines from affecting continuum parameters like the normalization and photon index. Afterwards, once the broadband continuum shape is well constrained, one can alter the binning to better resolve features like cyclotron lines.

I performed largely interactive spectral fitting which allowed parameter adjustment with immediate visual feedback in the spectral display. This interactive workflow was particularly useful for developing intuition about how individual spectral parameters and their combinations affect the continuum shape, especially when used with scripting for automation and repeatability.

3 Results

3.1 Spectral Parameter Results

In this section I present the unfolded spectra, fits, and fit parameters for the nine Sources I analyzed. I also discuss spectrum-specific model choices to motivate the post-unblinding interpretation (see Section 4). For display clarity, I binned the plotted data more coarsely than I did for the fitting analysis and, importantly, used a different statistical approach. These two approaches can yield different reduced chi-squared values for the same model. As such, the quoted χ^2_{red} values refer to the binning and statistics used during the analysis (and correspond to the reported model parameters), whereas the plotted data points and residuals reflect the display binning. Figure 7 is an example of the possible visual differences between the two schemes.

Being both spectrally "simple" and real, Sources 1 through 3 are better discussed in the context of the unblinded portion of the study, where my spectral fits can be compared to literature values (see Section 4). Nevertheless, I provide brief descriptions of my reasoning for the blinded portion of the analysis for those sources as well.

3.1.1 Source 1

Source 1 was adequately described by a cutoff powerlaw with no extra absorption features. While the residuals appeared to show extra components, particularly close to the soft X-rays, at the time I decided that these were particularly close to where the data were truncated. Moreover, an unfortunate over reliance on χ^2_{red} goodness-of-fit led me to conclude that the simplified model was sufficient. I discuss this further in the unblinded analysis.

3.1.2 Source 2

Source 2 stood out among all nine objects for its hard broadband continuum shape which did not require a cutoff. While this was confusing at the time and even led me to speculate that it might not be an accreting XRP, the reason for this is discussed in Section 4.

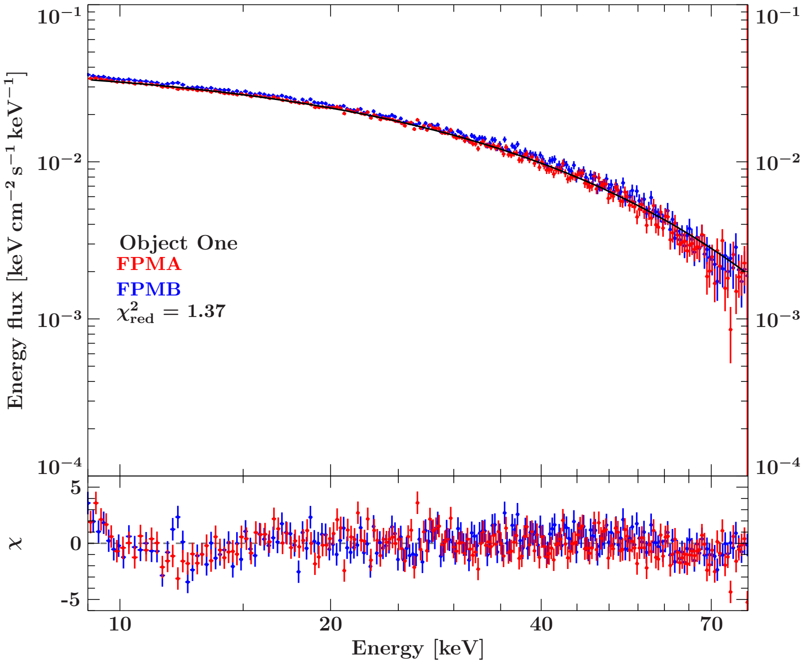

(a) Source 1

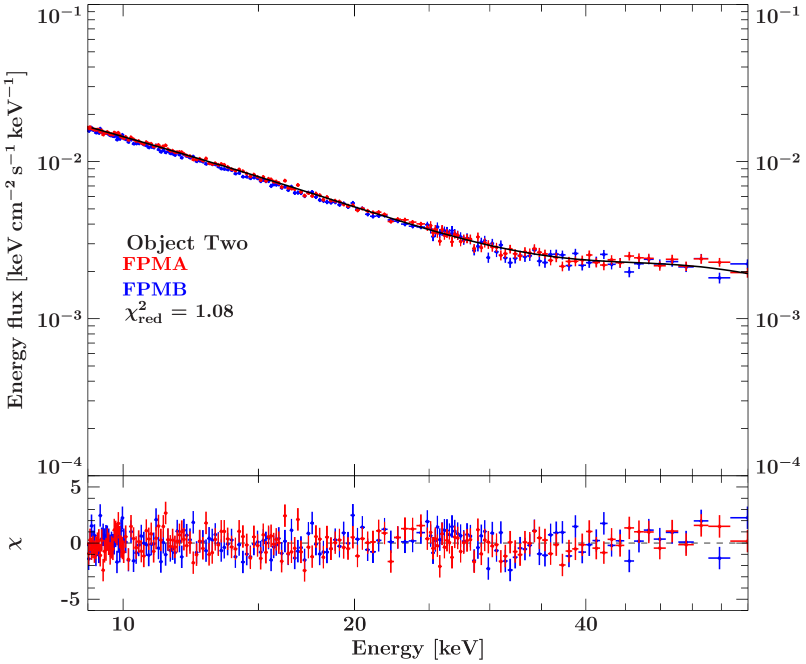

(b) Source 2

Figure 3: Spectra for Sources 1 and 2.

Table 1: Fit parameters for Sources 1 and 2 with models included.

Model	`detconst` × `cutoffpl`	`detconst` × (`powerlaw` × `gabs`)
Parameter	Source 1	Source 2
Detconst (FPMB)	1.042 ± 0.004	0.972 ± 0.005
Norm	0.0418 ± 0.0012	$0.282^{+0.025}_{-0.019}$
Photon Index	0.927 ± 0.015	$2.187^{+0.020}_{-0.019}$
HighECut	23.3 ± 0.4	—
LineE (gabs)	—	28.8 ± 0.7
Sigma (gabs)	—	$14.9^{+1.5}_{-1.3}$
Strength (gabs)	—	$19.4^{+3.7}_{-3.0}$

3.1.3 Source 3

Source 3 is the first source for which I fit the spectrum with a cutoff power law and an absorbed Gaussian component, as shown in the tables below. For the cutoff power law, I employed both `fdcut` and `cutoffpl`, ultimately adopting `fdcut` for its greater control over the cutoff energy, together with a single absorption-like feature at ∼16 keV.

3.1.4 Source 4

Source 4 exemplifies a recurring challenge. Namely, a pronounced dip in the broadband continuum can be interpreted in several ways: (i) a fairly steep energy cutoff, (ii) a broadened absorption-like feature, (iii) an emission feature preceding what would be the absorption-like feature under (ii) but might also be interpreted as the unaltered continuum, or (iv) an emission feature followed by a broadened absorption-like feature.

I tested each interpretation with the available models, tailoring initial cutoff power-law shapes and investigating the cutoff energy by fitting the soft portion of the spectrum with a simple power law to see where residuals began to diverge. Given the project's blinded nature, I relied primarily on residual behavior during fitting, along with goodness-of-fit and parameter minimization, rather than on physical intuition. Ultimately, the fourth scenario in combination with `fdcut` gave the best result; see Table 2 for details.

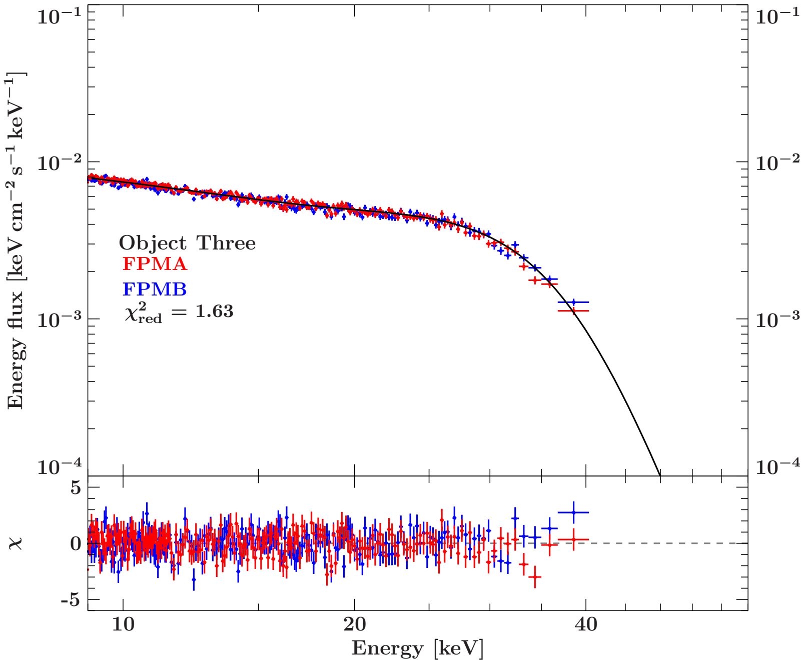

(a) Source 3

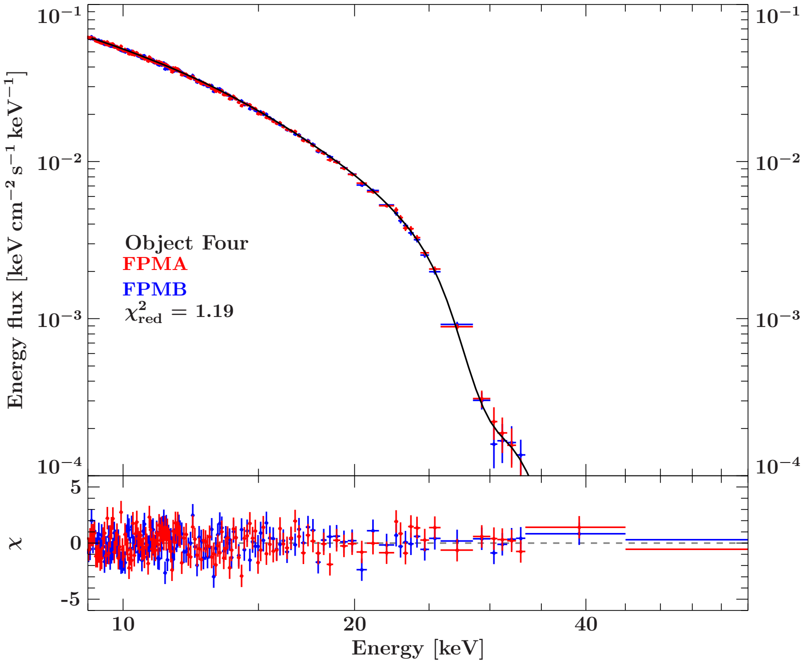

(b) Source 4

Figure 4: Spectra for Sources 3 and 4.

Table 2: Fit parameters for Sources 3 and 4 with models included.

Model	`detconst` × (`powerlaw` × `fdcut`) × `gabs`	`detconst` × (`powerlaw` × `fdcut` + `gaussian`) × `gabs`
Parameter	Source 3	Source 4
Detconst (FPMB)	$0.988^{+0.006}_{-0.007}$	$1.0010^{+0.0031}_{-0.0030}$
Norm (Powerlaw)	$0.0231^{+0.0038}_{-0.0027}$	1.1 ± 0.4
Photon Index	$1.47^{+0.06}_{-0.09}$	$2.20^{+0.17}_{-0.25}$
CutoffE	$34.1^{+0.8}_{-1.9}$	$14.1^{+1.7}_{-2.4}$
FoldE	$4.4^{+0.5}_{-0.4}$	$3.6^{+0.4}_{-0.8}$
LineE (gabs)	$16.7^{+0.6}_{-1.3}$	$29.4^{+0.9}_{-0.6}$
Sigma (gabs)	$5.0^{+2.9}_{-1.1}$	$2.1^{+0.6}_{-0.5}$
Strength (gabs)	$1.3^{+3.6}_{-0.6}$	$4.3^{+3.0}_{-1.7}$
Norm (Gaussian)	—	$\left(2.9^{+11.2}_{-1.6}\right) \times 10^{-3}$
LineE (Gaussian)	—	$17.0^{+2.4}_{-7.2}$
Sigma (Gaussian)	—	$5.2^{+2.1}_{-1.1}$

3.1.5 Source 5

Source 5 provides the clearest example of structures that could be cyclotron lines; I modeled these with `gabs`. Their energies and shapes, listed in Table 3, are suggestive of cyclotron harmonics. In this case, I made the decision to interpret these features as absorptive rather than emissive given they follow the pattern established by Source 4: systemic "wiggle"-like structures that appear in the residuals after fitting a cutoff powerlaw and are bisected by the model. From a purely phenomenological perspective, fitting these residual structures with three Gaussians yields equally good residuals and goodness-of-fit values. It is their apparent similarity to cyclotron harmonics (particularly given the energy spacing between them) that prompted my choice to use `gabs`.

3.1.6 Source 6

Source 6 proved more difficult. I tried four different fits using both powerlaw models in my toolkit, but the fit shown, marked by a relatively high reduced chi-squared, was the most satisfactory I could obtain. Replacing `cutoffpl` with `fdcut` did not improve the continuum modeling. All attempts at fitting the broadband continuum introduced structured "wiggle-like" residuals that were bisected by the model, which made it harder to distinguish absorption-like from emission-like structure.

To mitigate this, I varied the continuum rollover energy and photon index to steepen or flatten the slope, aiming to move the wiggles in the residuals above or below the model. I tested both scenarios and found the best result for this particular source when modeling two Gaussian emission components together with a single absorption feature; even so, some residual structure remained, hence the lower goodness-of-fit.

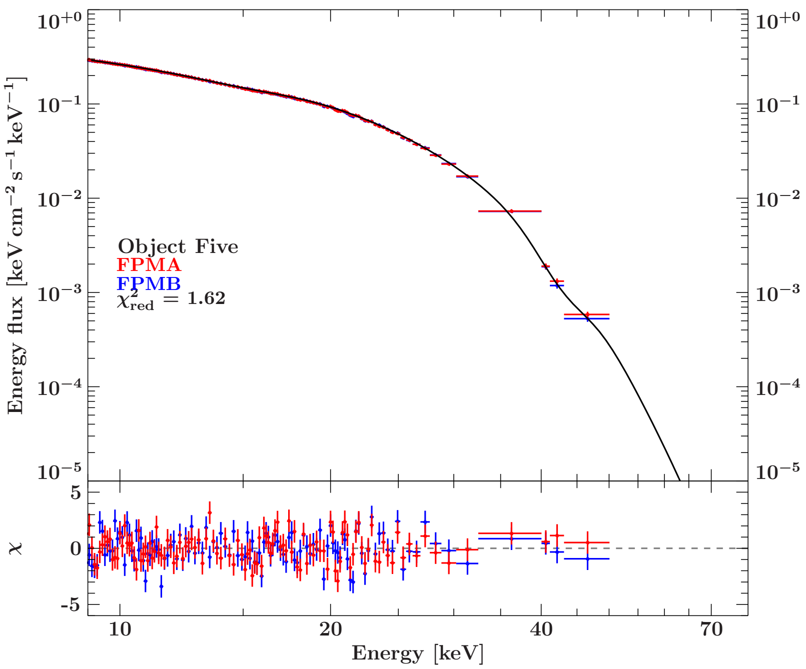

(a) Source 5

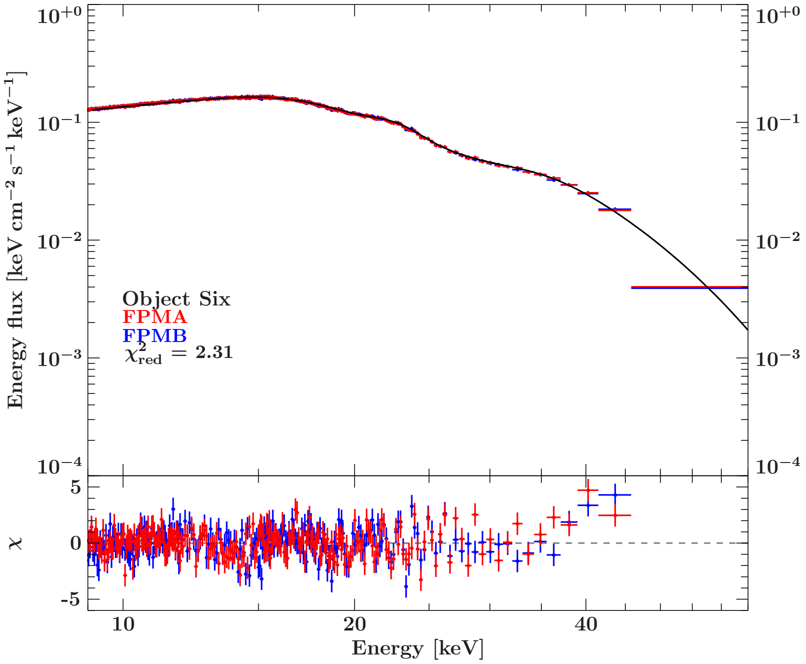

(b) Source 6

Figure 5: Spectra for Sources 5 and 6.

Table 3: Fit parameters for Sources 5 and 6 with models included.

Model	`detconst` × (`powerlaw` × `fdcut` × `gabs(1)` × `gabs(2)` × `gabs(3)`)	`detconst` × (`cutoffpl` + `gaussian(1)` + `gaussian(2)`) × `gabs`
Parameter	Source 5	Source 6
Detconst (FPMB)	0.9987 ± 0.0013	1.0002 ± 0.0014
Norm (Powerlaw)	$2.0^{+0.5}_{-0.6}$	$(6.93 \pm 0.10) \times 10^{-3}$
Photon Index	$1.84^{+0.11}_{-0.19}$	-0.907 ± 0.006
CutoffE	$27.5^{+3.3}_{-2.8}$	—
FoldE	$4.1^{+0.6}_{-0.5}$	—
LineE (gabs 1)	$14.68^{+0.16}_{-0.21}$	$27.57^{+0.30}_{-0.40}$
Sigma (gabs 1)	$2.43^{+0.36}_{-0.27}$	$4.71^{+0.28}_{-0.25}$
Strength (gabs 1)	$0.57^{+0.29}_{-0.15}$	$3.77^{+0.31}_{-0.25}$
LineE (gabs 2)	$27.9^{+3.4}_{-3.0}$	—
Sigma (gabs 2)	$8.1^{+1.0}_{-1.2}$	—
Strength (gabs 2)	12^{+11}_{-7}	—
LineE (gabs 3)	$42.6^{+1.2}_{-1.0}$	—
Sigma (gabs 3)	$3.5^{+0.9}_{-0.8}$	—
Strength (gabs 3)	$4.5^{+2.9}_{-1.9}$	—
Norm (Gaussian 1)	—	$0.0117^{+0.0011}_{-0.0008}$
LineE (Gaussian 1)	—	$15.13^{+0.15}_{-0.12}$
Sigma (Gaussian 1)	—	$2.78^{+0.12}_{-0.10}$
Norm (Gaussian 2)	—	$\left(3.0^{+0.8}_{-0.7}\right) \times 10^{-3}$
LineE (Gaussian 2)	—	22.50 ± 0.07
Sigma (Gaussian 2)	—	1.60 ± 0.13

3.1.7 Sources 7, 8, & 9

Sources 7, 8, and 9 were also broadly similar to Source 4. For this reason, I group them in this section. The fitting approach for Sources 7 and 9 closely followed that of Source 4, though with somewhat higher final χ^2_{red} values. Source 8 required more manual fitting to achieve a realistic cutoff energy. Both it and source 7 also exhibited what I identified as the most obvious cases of a 10 keV feature. This is shown by the Gaussians I use in the sources' models and their parameters, displayed in Table 6.

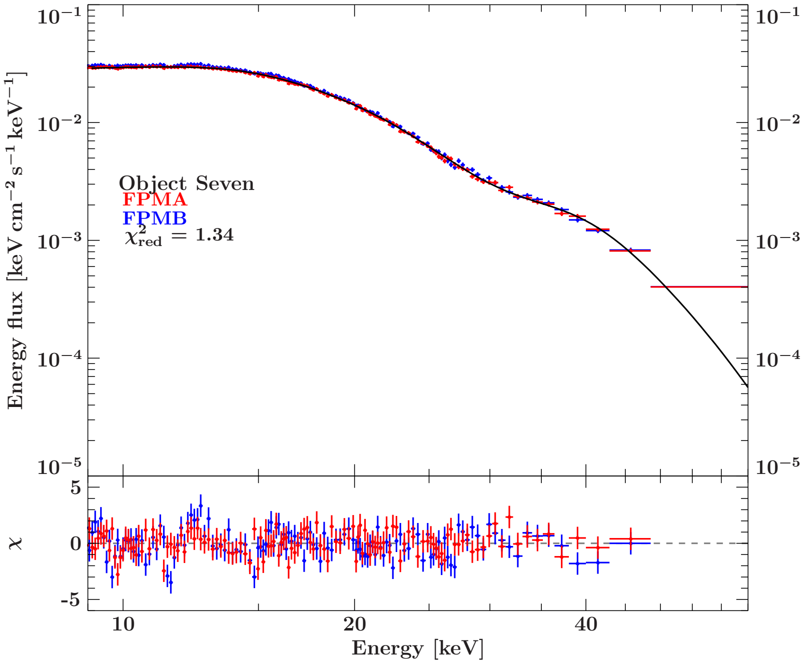

(a) Source 7

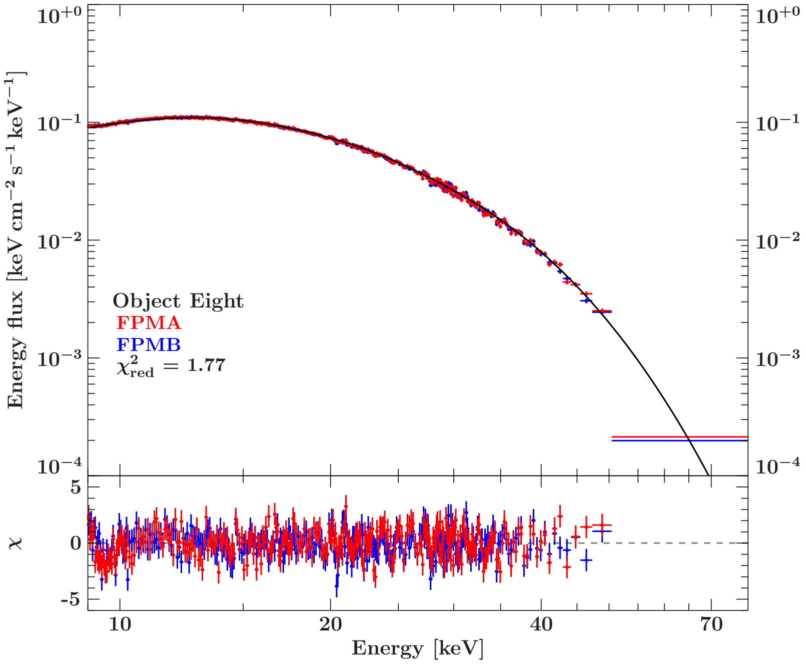

(b) Source 8

Figure 6: Spectra for Sources 7 and 8.

Table 4: Fit parameters for Sources 7 and 8 with models included.

Model	`detconst` × (`powerlaw` × `fdcut` + `gaussian`) × `gabs(1)`	`detconst` × (`powerlaw` × `fdcut` + `gaussian`) × `gabs(1)`
Parameter	Source 7	Source 8
Detconst (FPMB)	1.034 ± 0.004	1.0003 ± 0.0017
Norm (Powerlaw)	$0.035^{+0.016}_{-0.010}$	$\left(3.9^{+2.1}_{-1.4}\right) \times 10^{-3}$
Photon Index	1.0 ± 0.4	-0.8 ± 0.4
CutoffE	11^{+9}_{-11}	9 ± 4
FoldE	$9.0^{+0.8}_{-0.9}$	5.40 ± 0.24
Norm (Gaussian 1)	$0.013^{+0.006}_{-0.005}$	$\left(2.4^{+4.0}_{-1.0}\right) \times 10^{-3}$
LineE (Gaussian 1)	11.0 ± 0.9	$12.07^{+0.22}_{-0.37}$
Sigma (Gaussian 1)	$5.1^{+0.6}_{-0.7}$	$2.0^{+0.6}_{-0.4}$
LineE (gabs)	30.0 ± 0.5	$25.0^{+1.4}$
Sigma (gabs)	$3.7^{+0.7}_{-0.6}$	$10.0^{+0.0}_{-2.1}$
Strength (gabs)	$2.4^{+1.7}_{-1.0}$	$5.9^{+2.0}_{-3.1}$

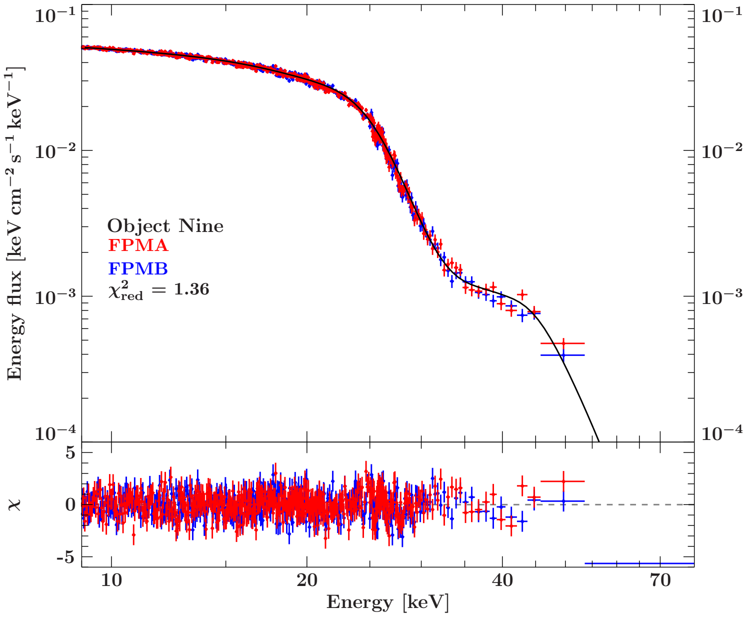

(a) Source 9 (display binning)

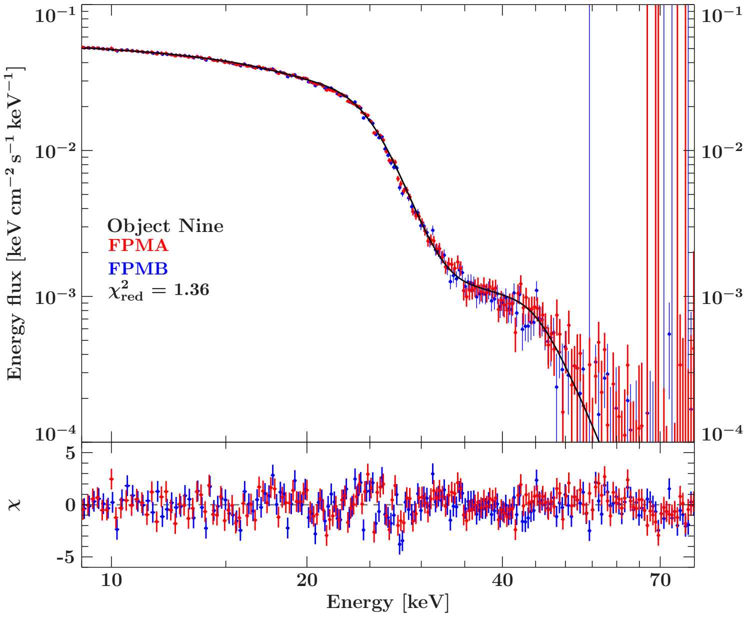

(b) Source 9 (fit analysis binning)

Figure 7: Spectra of Source 9. Left shows display binning whereas right shows fit analysis binning.

Table 5: Fit parameters for Source 9 with model included.

Model	`detconst` × (`powerlaw` × `fdcut` + `gaussian`) × `gabs`
Parameter	Source 9
Detconst (FPMB)	0.9981 ± 0.0026
Norm (Powerlaw)	$0.087^{+0.009}_{-0.008}$
Photon Index	1.22 ± 0.05
CutoffE	$25.2^{+2.0}_{-1.4}$
FoldE	$5.38^{+0.19}_{-0.28}$
Norm (Gaussian 1)	$\left(1.8^{+0.7}_{-0.6}\right) \times 10^{-3}$
LineE (Gaussian 1)	23.78 ± 0.18
Sigma (Gaussian 1)	$2.46^{+0.21}_{-0.29}$
LineE (gabs)	$33.36^{+0.29}_{-0.28}$
Sigma (gabs)	5.9 ± 0.5
Strength (gabs)	$23.0^{+4.1}_{-2.9}$

4 Discussion

4.1 Unblinding

The unblinding procedure entailed revealing the synthetic nature of five out of the nine spectra I observed, the physical model used to generate the spectral shapes, and the goal of the study: an unbiased characterization of synthetic spectra generated using a model that incorporates thermal resonant Comptonization. The spectra were truncated to focus on intermediate and hard X-ray energies, where cyclotron lines are most commonly observed in highly magnetized sources. Further, at lower energies, the synthetic spectra deviate from real observations, as they do not include interstellar absorption or the reprocessing that produces the characteristic soft X-ray iron emission line.

Sources 1, 2, 3, and 7 are real and correspond to KS 1947+300 (a BeXRB), X Per (a BeXRB), A 0535+262 (a BeXRB), and Cen X-3 (an SgXRB), respectively. The remaining sources are synthetic and their spectral parameters are shown in Table 6. Figures 8 through 10 show plots of the synthetic sources' models.

Table 6: Physical parameters for all synthetic Sources.

Parameter	Source 4	Source 5	Source 6	Source 8	Source 9
kT_e (keV)	4	6	7	8	6
$E_{\rm cyc}$ (keV)	40	60	30	100	40
$\tau_{\rm T}$	500	500	500	500	500

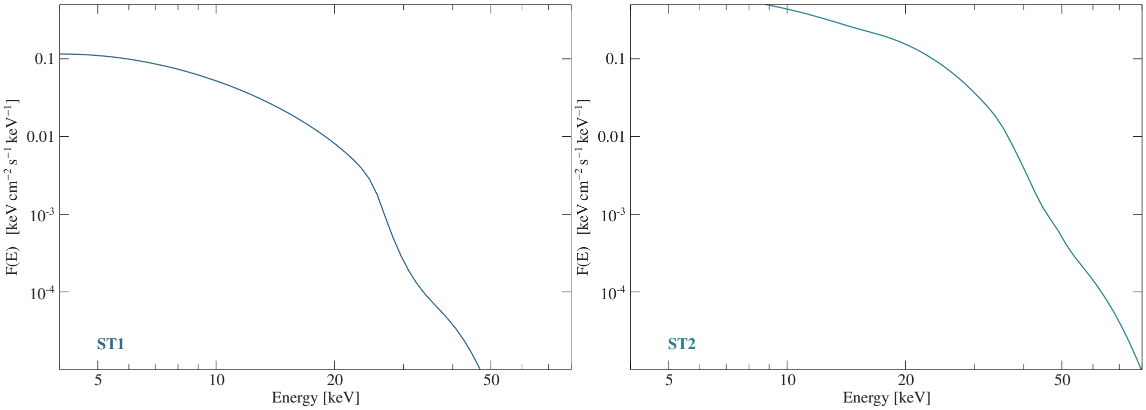

(a) Source 4 physical model.

(b) Source 5 physical model.

Figure 8: Physical models for Sources 4 and 5.

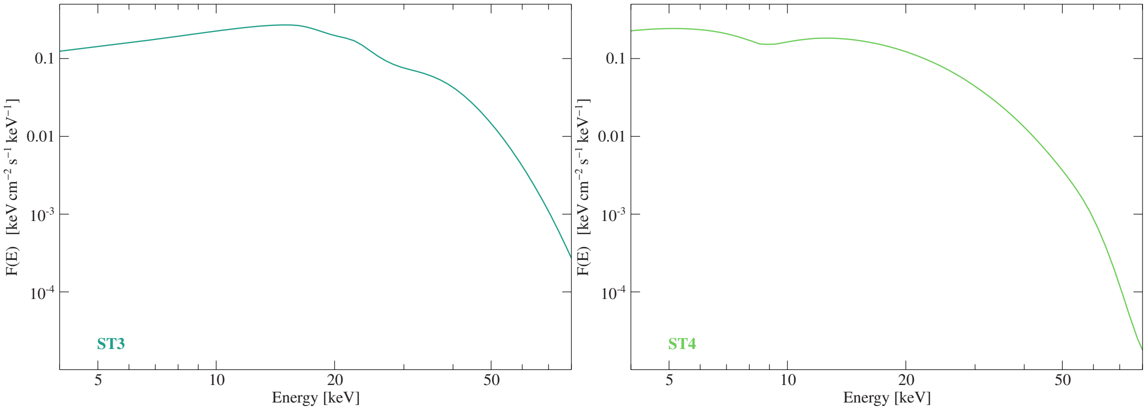

(a) Source 6 physical model.

(b) Source 8 physical model.

Figure 9: Physical models for Sources 6 and 8.

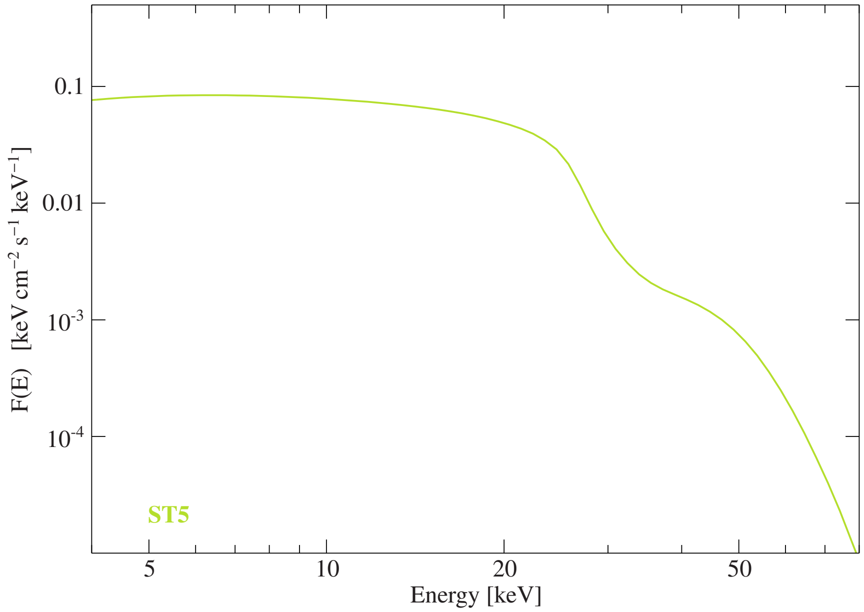

Figure 10: Source 9 physical model.

4.2 Physical Continuum Modeling

The synthetic spectra analyzed here were produced using an adaptation of the Sokolova-Lapa et al. (2023) physical model for the homogeneous atmosphere case. This physical model, `sigel-T`, accounts for vacuum polarization effects on accreting XRP polar emission together with magnetic Comptonization, with particular attention to cyclotron-line shape. Motivated by Meszaros & Nagel (1985a,b) on the influence of vacuum and plasma polarization modes in homogeneous media, Sokolova-Lapa et al. developed a slab geometry model that incorporates vacuum and plasma polarization effects, thermal resonant Comptonization, and bremsstrahlung. For this study, the spectra were generated using a simpler realization of the model that integrates over all angles and does not account for geometry and light bending. Different spectra were generated by varying normalization, electron temperature, electron number density, cyclotron energy, and optical depth.

4.3 Real Source Comparative Analysis

I worked through the nine sources sequentially, as they were not all assigned to me at the same time. As a result, Source 1 reflects some of my earliest work on the project, while the later objects benefited from greater familiarity with fitting procedures. Although I revisited the earlier sources later in the study, I choose to present the results chronologically, as this ordering more clearly illustrates both the pedagogical progression and the scientific development of the analysis.

4.3.1 Source 1

Source 1 (KS 1947+300) presented a spectrum that could be fit with a single cutoff power-law model with what appeared to be reasonable parameters (see Fig. 3 and Table 1). In retrospect, it is clearer that the residual structure suggests the presence of a broadened absorption-like feature centered at approximately 12.5 keV, which is generally accepted as a cyclotron line in the literature (Fürst et al. 2014). At the time, I did not model this feature, largely due to an over-reliance on the reduced chi-squared value relative to the residual structure. In particular, fitting this structure in the residuals led to a decrease in χ^2_{red} of only $\sim$0.15, which I interpreted as indicative of overfitting. I later recognized that this criterion was too conservative and that, while minimizing degrees of freedom remains important, greater weight should be given to the shape of the residuals in conjunction with the overall unreduced χ^2 values.

4.3.2 Source 2

Source 2 (X Per) also proved challenging, as it ran counter to a naive expectation based on "canonical" accreting XRP phenomenological modeling. In particular, the source showed no evidence of a high-energy cutoff within *NuSTAR*'s energy range and was instead best described by a hard power-law continuum. Nevertheless, I identified an absorption feature at approximately 29 keV which was identified as a CRSF as early as 2001 (Coburn et al. 2001). This, however, is no longer believed to be a CRSF, but the dip between continuum components making up the characteristic double hump structure one would expect from low-luminosity sources, as discussed in 1.1.3 (Sokolova-Lapa et al. 2021; Tsygankov et al. 2019; Mushtukov et al. 2021).

4.3.3 Source 3

Source 3 (A 0535+262) required stronger binning than the previous real sources, as well as cutting data above 60 keV, so the analyzed energy range is smaller compared to the other sources. Given that the source observation I used was taken at a low luminosity, the 16 keV absorption feature most likely shows the evolving double hump structure. Rather, this source has a well-established CRSF at $\sim$ 45 keV (Tsygankov et al. 2019; Ballhausen et al. 2017). Moreover, by looking at a more recent lower-luminosity observation of A 0535+262, Tsygankov et al. (2019) show that the source shows no positive correlation between cyclotron line energy and mass accretion rate for pulse-averaged spectra.

4.3.4 Source 7

Finally, Source 7 (Cen X-3) exhibits a spectral shape and behavior similar to those of several synthetic sources I analyzed. As shown in Table 4, I identify a broadened absorption feature at 30 keV, consistent with the canonically well-established CRSF at $\sim$ 30 keV (Nagase et al. 1992; Santangelo et al. 1998).

4.4 Unblinded Analysis: Fit Comparison with Model-Defined Input Parameters

I was able to recover the model-defined input parameters consistently with my fits, but achieving acceptable fit statistics introduced additional absorption and emission structure in the residuals. This is most apparent for Source 6. Further, the fitting dilemma I discuss in Section 3 for Source 4 and similar objects appears to stem from the intrinsic model's cyclotron-line red wing, which is caused by photon redistribution via resonant scattering and energy-dependent polarization-mode contributions. This wing appears, from a purely phenomenological perspective, as a broad emission component preceding a broadened absorption-like feature, and so may be consistent with a variety of physical interpretations when seen that way.

Because some cyclotron lines were located above the detection threshold at the observed flux (e.g., Source 5's ~ 60 keV feature), fitting an otherwise ostensibly featureless continuum produced, in Source 5's case, three weak absorption-like features (Table 3) that resemble, and could therefore be interpreted as, CRSF harmonics given their energy spacing of $\sim 14\,\mathrm{keV}$. In short, standard fitting approaches can introduce artificial features that are readily misinterpreted.

I estimated electron temperatures from fit parameters using equation 1 in Meszaros & Nagel (1985b),

$$\left(\frac{\Delta\omega}{\omega_B}\right)_{\mathrm{FWHM}} = \left(\frac{8\ln 2\, kT_e}{m_e c^2}\right)^{1/2} \cos\theta, \tag{7}$$

which describes the thermal Doppler broadening of cyclotron lines. Assuming the identified absorption features are CRSFs and adopting $\theta = 45°$, I approximate the cyclotron lines' full width at half maximum (FWHM) and use the equation to calculate the electron temperature kT_e. I present results for a selection of synthetic sources for comparison with the model-defined input parameters.

Approximating the FWHM produced reasonable estimates of kT_e when compared with the input physical parameters in Table 6. Estimating Source 4's FWHM as $\sim 10\,\mathrm{keV}$ yielded $kT_e = 7.4\,\mathrm{keV}$; Source 6's FWHM as $\sim 7\,\mathrm{keV}$ yielded $kT_e \sim 12\,\mathrm{keV}$; and Source 5's first (false) harmonic with FWHM $\sim 5\,\mathrm{keV}$ yielded $kT_e \sim 21\,\mathrm{keV}$, while the higher-energy harmonics yielded electron temperatures between 3 and $6\,\mathrm{keV}$.

Notably, using the model-defined `gabs` line width parameter (σ) values instead of the approximate FWHM systematically produced electron temperature values up to four times higher than expected. Staubert et al. (2019) point out that the `gabs` model's Gaussian profile arises from the Maxwellian distribution of thermal electron velocities as derived from the transfer equations in the case of *true absorption lines*, which cyclotron lines are not. As such, they argue that the `gabs` function should be considered purely phenomenological in the case of CRSFs. Moreover, variation in observer viewing angle and XRP pole location contributes to the phase-averaged CRSF profile, such that there will always be notable uncertainty in the determined plasma temperature, even under the assumption of purely thermal broadening.

5 Conclusions

By comparing unbiased phenomenological fit parameters to known model-defined input parameters for synthetic spectra, this study has shown that adequately fitting the accreting XRP continua examined here often required artifactual emission and absorption-like features, which manifest prominently in the residuals. For example, in Source 4 and several subsequent cases, fitting the model-defined cyclotron line necessitated a broad emission component immediately preceding the CRSF. This apparent emission arises naturally from photon redistribution into the CRSF's red wing and energy-dependent polarization mode contributions. Source 5 provides a particularly illustrative case: a featureless continuum within *NuSTAR*'s energy range, given sufficient signal-to-noise, produced pronounced residual structures when fit with a simple cutoff power law. These structures, spaced roughly 14 keV apart, closely mimic cyclotron line harmonics. Source 6 showed similar behavior, though complicated by the presence of a model-defined CRSF at 30 keV. These examples demonstrate that standard fitting approaches can introduce spurious features, which would only be further complicated by relativistic effects.

Overall, this project's results emphasize the necessity of physically consistent models to bridge the gap between theory and observation. Reliance on phenomenological fitting alone risks attributing instrumental or fitting artifacts to genuine spectral features, potentially skewing interpretation and conclusions. Distinguishing spectral features arising from the limitations of phenomenological fitting from those tracing genuine physical processes like polarization effects will be vital to understanding the physics behind accreting XRP magnetic fields and emission geometries.

Bibliography

Ballhausen R., Pottschmidt K., Fürst F., et al., 2017, A&A 608, A105

Basko M.M., Sunyaev R.A., 1975, A&A 42, 311

Basko M.M., Sunyaev R.A., 1976, MNRAS 175, 395

Becker P.A., Klochkov D., Schönherr G., et al., 2012, A&A 544, A123

Becker P.A., Wolff M.T., 2007, ApJ 654, 435

Caballero I., Wilms J., 2012, Mem. Soc. Astron. It. 83, 230

Coburn W., Heindl W.A., Gruber D.E., et al., 2001, ApJ 552, 738

Davidson K., Ostriker J.P., 1973, ApJ 179, 585

Falkner S., 2018, Ph.D. thesis, Friedrich-Alexander-Universität Erlangen-Nürnberg, Erlangen

Fürst F., Pottschmidt K., Wilms J., et al., 2014, ApJ 784, L40

Ghosh P., Lamb F.K., 1979, ApJ 234, 296

Laurent P., Titarchuk L., 1999, ApJ 511, 289

Lorimer D.R., Kramer M., 2012, Handbook of Pulsar Astronomy, Cambridge University Press, Cambridge, UK

Meszaros P., Nagel W., 1985a, ApJ 298, 147

Meszaros P., Nagel W., 1985b, ApJ 299, 138

Mihara T., 1995, Ph.D. thesis, University of Tokyo, Tokyo

Mihara T., Makishima K., Nagase F., 2004, ApJ 610, 390

Müller S., Ferrigno C., Kühnel M., et al., 2013, A&A 551, A6

Mushtukov A., Tsygankov S., 2024, Accreting Strongly Magnetized Neutron Stars: X-ray Pulsars. In: Bambi C., Santangelo A. (eds.) Handbook of X-ray and Gamma-ray Astrophysics. Springer Nature Singapore, Singapore, p. 138

Mushtukov A.A., Suleimanov V.F., Tsygankov S.S., Portegies Zwart S., 2021, MNRAS 503, 5193

Nagase F., Corbet R.H.D., Day C.S.R., et al., 1992, ApJ 396, 147

Nagel W., 1980, ApJ 236, 904

Nagel W., 1981, ApJ 251, 288

Nishimura O., 2005, PASJ 57, 769

Santangelo A., del Sordo S., Segreto A., et al., 1998, A&A 340, L55

Schönherr G., Schwarm F.W., Falkner S., et al., 2007, A&A 597, 353

Schwarm F.W., 2017, Ph.D. thesis, Friedrich-Alexander-Universität Erlangen-Nürnberg, Erlangen

Schwarm F.W., Ballhausen R., Falkner S., et al., 2017a, A&A 601, A99

Schwarm F.W., Schönherr G., Falkner S., et al., 2017b, A&A 597, A3

Sokolova-Lapa E., Gornostaev M., Wilms J., et al., 2021, A&A 651, A12

Sokolova-Lapa E., Stierhof J., Dauser T., Wilms J., 2023, A&A 674, L2

Staubert R., Trümper J., Kendziorra E., et al., 2019, A&A 622, A61

Tanaka Y., 1986, In: Mihalas D., Winkler K.H.A. (eds.) Radiation Hydrodynamics in Stars and Compact Objects, 255. Lecture Notes in Physics, Springer Berlin, Heidelberg, p. 198

Trümper J., Pietsch W., Reppin C., et al., 1978, ApJ 219, L105

Tsygankov S.S., Doroshenko V., Mushtukov A.A., et al., 2019, MNRAS 487, L30

Wilms J., 2014, In: Bozzo E., Kretschmar P., Audard M., Falanga M., Ferrigno C. (eds.) European Physical Journal Web of Conferences, 64. European Physical Journal Web of Conferences, EDP, p. 06001